Synthesis of Co–Ni and Cu–Ni based-catalysts for dry reforming of methane as potential components for SOFC anodes

Moisés Cesario, Glageane Souza, Francisco J.A. Loureiro, Allan J.M. Araújo, João P.F. Grilo, Samer Aouad, Daniel Macedo, Duncan Fagg, Haingomalala Lucette Tidahy, Cédric Gennequin, et al.

Version of Record: https://www.sciencedirect.com/science/article/pii/S0272884221026225
Manuscript_f614f82d357515f601a90130e8d15318

Synthesis of Co-Ni and Cu-Ni based-catalysts for dry reforming of methane as potential components for SOFC anodes

Moisés R. Cesario[a,b*], Glageane S. Souza[b,c], Francisco J. A. Loureiro[d], Allan J. M. Araújo[d,e], João P. F. Grilo[f], Samer Aouad[g], Haingomalala L. Tidahy[a], Daniel A. Macedo[b], Duncan P. Fagg[d], Cédric Gennequin[a], Edmond Abi-Aad[a]

[a]Unité de Chimie Environnementale et Interactions sur le Vivant (UCEIV, U.R. 4492), MREI, Université du Littoral Côte d'Opale (ULCO), 59140 Dunkerque, SFR Condorcet FR CNRS 3417,France

[b]Materials Science and Engineering Postgraduate Program, Federal University of Paraíba, 58051-900, João Pessoa, Brazil

[c]Academic Unit of Physics and Mathematics, Federal University of Campina Grande, 58750-000, Cuité, Brazil

[d]Centre of Mechanical Technology and Automation, Department of Mechanical Engineering, University of Aveiro, 3810-193, Aveiro, Portugal

[e]Materials Science and Engineering Postgraduate Program (PPGCEM), Federal University of Rio Grande do Norte (UFRN), 59078-970, Natal, Brazil

[f]Department of Materials and Ceramic Engineering/CICECO, University of Aveiro, Aveiro, Portugal

[g]Department of Chemistry, Faculty of Arts and Sciences, University of Balamand, El Kurah, North Lebanon, P.O: box 100, Tripoli, Lebanon

Abstract

In this work, we report a comparative study of Ni-based anode compositions, made of Cu and Co (40 and 80 mol%) and gadolinia-doped ceria (CGO) matrices, for application the dry reforming of methane (DRM) reaction using Solid Oxide Fuel Cells (SOFCs). The new compositions are synthesized by a one-step synthesis route, using citric acid as chelating agent, and characterized at three different stages: i) after synthesis, ii) after reduction, and iii) after DRM. X-ray diffraction (XRD) analysis combined with thermodynamic calculations is used to understand phase evolution along the different stages, revealing that complete solid solutions of NiCo- and

NiCu-based alloys are formed after DRM reaction. Transmission Electron Microscopy (TEM) shows the formation of nanocrystalline powders, while surface area (S_{BET}) measurements show higher values in the case of the NiCo-based samples. Moreover, the Co-containing compositions exhibit higher reducibility and stronger metal-ceramic interactions than the Cu-containing samples, according to the Temperature Programmed Reduction (TPR) results. Finally, DRM results demonstrate higher CO_2 and CH_4 conversions in the case of the Co-containing samples, as well as increased resistance towards carbon deposition, as confirmed by Thermogravimetric and Differential Scanning Calorimetry analyses (TG-DSC). Overall, the Co-based compositions are highly beneficial for their use as anodes for the CO_2 reforming of methane in SOFCs.

Keywords: One-step synthesis; cermet anode; Solid Oxide Fuel Cell (SOFC); Gadolinia-doped Ceria (CGO); Nickel alloy

***Corresponding authors: moisesrcesario@gmail.com

1. Introduction

The search for new clean energy sources with a significant reduction of greenhouse gas emissions like carbon dioxide (CO_2) and methane (CH_4) has been strongly encouraged. One of the most promising and exciting uses of these gases is in the dry reforming of methane (DRM), where CO_2 is used as a reforming agent (Eq. 1) [1–4].

$$CH_4 + CO_2 \rightarrow 2CO + 2H_2 \quad \Delta H_{298K} = 247 \text{ kJ mol}^{-1} \tag{1}$$

With this technology, a syngas product is obtained, with an equimolar mixture of hydrogen (H_2) and carbon monoxide (CO), suitable for preparing a large variety of chemicals such as acetic acid, ammonia, or methanol. However, this reaction is highly endothermic, requiring the use of high temperatures and low pressures for good conversions of methane [5,6].

This problem can be partially mitigated by using electrochemical membrane reactors, which combine reaction and selective separation through the electrolyte membrane, helping to forward the reaction [7,8]. Moreover, syngas production by electrochemical routes is a desirable green alternative when the CH_4 can be reformed *in situ* using renewable electricity [9,10]. Hence, these systems can offer a significant cost saving since a considerable fraction of the cost of current industrial processes lies in hydrogen production and its subsequent purification.

One of the most promising electrochemical systems is based on the solid-state oxide-ion (O^{2-}) conductors using Solid Oxide Fuel Cells (SOFCs). Such devices can operate at high temperatures, *i.e.*, above 600 °C, where the DRM reaction becomes favored. Thus, oxide-ion-conducting materials become highly relevant at these temperatures due to their very high conductivity under such conditions (≥ 0.01 S cm^{-1}) [11].

Cerium oxide is well-known for its fluorite-type structure, with a large tolerance for high levels of atomic disorder, which can be introduced either by doping, reduction, or oxidation. The addition of dopants, such as trivalent rare earth cations, Gd_2O_3 for example, to CeO_2 results in

the creation of charge-compensating oxygen vacancies, promoting the mobility of oxygen ions, according to Eq. 2 in Kröger-Vink notation, as well as the creation of basic sites that improve the CO_2 adsorption on the support [11–13].

$$Gd_2O_3 \xrightarrow{CeO_2} 2Gd'_{Ce} + 3O_O^x + V_O^{\bullet\bullet} \quad (2)$$

In addition to the ceramic oxide-ion phase, the cermet anode must include a metallic components that serves as a catalyst while providing also electronic conductivity.

In this respect, nickel-based catalysts have been widely investigated for the DRM reaction due to their high catalytic activity, selectivity, and low-cost [14–18]. However, Ni catalysts also have an increased susceptibility to deactivation by carbon deposition and sintering [14–18]. Following the traditional literature from the catalysis field, one can realize the beneficial effect of alloying with different transition metals to enhance the catalytic properties of Ni catalysts towards CO_2 reforming of methane. In this respect, several attention has been given to Co and Cu as promoters to the nickel component [19–22].

In electrochemical systems, such as the SOFC technology, few studies have previously focused on the influence of copper and cobalt additions using ceria–gadolinia (CGO) matrices. For example, Loureiro *et al.* [17] highlighted that adding copper to nickel could promote increased stability against carbonation. In another work, Sarruf *et al.* [23] reported a nickel-free SOFC anode (based on Co-Cu alloys) operating with high performance with direct methane.

While most studies focus on electrochemical performance, a crucial step before implementing fuel processing reactions is to understand the catalytic activity of the materials towards the DRM reaction. In this respect, the reducibility of multicomponent phases and metal-ceramic interactions are among the most critical factors that can influence the catalytic properties of the cermet anodes [24,25]. Therefore, studying these features before implementation in real

electrochemical systems is crucial for developing proper electrode materials that must offer good electrochemical performance and enhanced catalytic activity.

To this end, the effect of the powder synthesis method on the physicochemical properties of the cermet anode may be a critical step to design suitable components.

Among the different synthetic chemical routes, a one-step synthesis method has been of particular interest, in which resins are obtained from polymeric precursors, using citric acid as a chelating agent. This method is based on the *Pechini* method, through condensation reactions using a hydroxycarboxylic acid (*e.g.*, citric acid) combined with a polyhydroxy alcohol (*e.g.*, ethylene glycol). *Pechini* method involves two essential reactions: chelation between complex cations and acid citric, leading to metallic citrate, and polyesterification reaction with ethylene glycol, obtaining a polyester resin. The resins are thermally treated to directly produce composite powders, as it was recently reported for the preparation of NiO- and CuO-ceria-based anode precursor powders for Solid Oxide Fuel Cells (SOFCs) [18,26–30]. The current authors successfully modified this method to synthesize $Ni_{1-x}Cu_xO$-$Ce_{0.9}Gd_{0.1}O_{2-\delta}$ (CGO) precursor powders, providing a further anode compositional range for solid oxide fuel cells running on hydrogen and biogas [17]. Here, we return to this one-step synthesis method to systematically study the effects of both cobalt and copper additions on the structure and performance of Ni-based CGO anode powders towards the dry reforming of methane (DRM) reaction.

2. Experimental

2.1.Synthesis and characterization

NiO-CGO, (Ni,Co)O-CGO (40 and 80 mol% CoO) and (Ni,Cu)O-CGO (40 and 80 mol% CuO) powders (with 50 wt% CGO ($Ce_{0.9}Gd_{0.1}O_{1.95}$)) were prepared by the one-step synthesis route [26]. The precursor powders were obtained after a single heat treatment at 350 °C. The precursor resins of the NiO, (Ni,Co)O, (Ni,Cu)O, and CGO phases were firstly synthesized in separated containers, each of them containing previously dissolved citric acid ($[C_6H_8O_7.H_2O]$) into distilled water at 50 °C.

In the case of the cerium citrate solution, cerium nitrate [$Ce(NO_3)_3.6H_2O$] was dissolved into distilled water and further complexing with citric acid [$C_6H_8O_7.H_2O$] at 65-70 °C, using a cation/citric acid molar ratio of 1/3.5. Afterward, gadolinium nitrate [$Gd(NO_3)_3.6H_2O$] was added in stoichiometric amounts after stirring for 30 min at 65-70 °C. The resulting solution was kept at this temperature range for 1 h to form chelate cations. Then, to promote the esterification reaction, ethylene glycol [$C_2H_6O_2$] was added in the weight ratio of 60:40 (citric acid: ethylene glycol), and the temperature was increased to 75-80 °C. The resulting solution was maintained under stirring and heating at 75-80 °C for 2 h to remove the excess water and to form the precursor resin of the CGO phase.

In a second beaker, the precursor resin of the NiO phase was synthesized. Nickel nitrate [$Ni(NO_3)_2.6H_2O$] was used as the source of Ni, and the same proportions of metal/citric acid and citric acid/ethylene glycol adopted in the synthesis of CGO were used. The NiO precursor resin was poured into the beaker containing the CGO precursor resin, and the resulting solution was mixed at room temperature for about 5 min, resulting in a homogeneous resin containing Ce, Gd, and Ni cations. The same experimental procedure was used to obtain powders of $Ni_{1-x}Co_xO$-CGO and $Ni_{1-x}Cu_xO$-CGO (x = 0.4 and 0.8) using cobalt and copper nitrates. All chemicals were used as purchased from Sigma-Aldrich. The resulting resins were heat-treated at

350 °C in air for 1 h using a heating rate of 1 °C min^{-1} to produce the so-called precursor powders, which were further calcined at 700 °C for 1 h. All synthesized materials are listed in Table 1.

Table 1 – Nomenclature adopted for all synthesized materials.

Material	Nomenclature
50 wt% (NiO) + 50 wt% (CGO)	Ni-CGO
50 wt% (60 mol% NiO + 40 mol% CoO) + 50 wt% (CGO)	$Ni_{0.6}Co_{0.4}$-CGO
50 wt% (20 mol% NiO + 80 mol% CoO) + 50 wt% (CGO)	$Ni_{0.2}Co_{0.8}$-CGO
50 wt% (60 mol% NiO + 40 mol% CuO) + 50 wt% (CGO)	$Ni_{0.6}Cu_{0.4}$-CGO
50 wt% (20 mol% NiO + 80 mol% CuO) + 50 wt% (CGO)	$Ni_{0.2}Cu_{0.8}$-CGO

The calcined and reduced samples were characterized by X-ray diffractometry (XRD) using a Bruker D8-Advance diffractometer, with Cu Kα radiation (λ=1.5406 Å), at room temperature. The diffraction powder patterns were obtained in the angular range of 10–90° 2θ using step-scanning mode (0.02° $step^{-1}$) with a counting time of 2 s $step^{-1}$. Rietveld refinement was carried out using a Rigaku SmartLab Studio II software, using a pseudo-Voigt peak profile function for the profile fitting and the the B-spline function for the background fitting.

The specific surface area employing the BET method (Brunauer, Emmett, and Teller) was determined by N_2 adsorption-desorption at -196 ºC in a Quanta Sorb Junior analyzer. The samples were degassed for 30 min at 150 °C before being analyzed.

Temperature-programmed reduction (TPR) was carried out on an Altamira AMI 200 apparatus to study the reducibility of the samples. A mass of 10-20 mg was placed in a quartz U-tube (4

mm internal diameter) and pretreated under Ar (30 mL min^{-1}) from room temperature to 150 °C for 30 min. The samples were cooled and then heated to 900 °C (using a heating rate of 5 °C min^{-1}) in a mixture of 95% argon and 5% hydrogen under a total gas flow of 30 mL min^{-1}. When convenient, Scanning and Transmission Electron Microscopy (STEM) was carried out in a Hitachi HD-2700 equipment to characterize the morphology of the reduced particles.

The spent samples were characterized by XRD and thermogravimetry/differential scanning calorimetry (TG-DSC). TG-DSC analyses were performed in air (75 ml min^{-1}) from room temperature to 1000 °C with a heating rate of 5 °C min^{-1} using a Netzsch STA 409 apparatus.

2.2.Catalytic tests

The catalytic activity was evaluated in the dry reforming of methane reaction under atmospheric pressure. The powders were pelletized, crushed and sieved. The size fraction between 350 μm and 800 μm was chosen for sieving to prevent mass and heat transfer limitations [31]. Around 100 mg of the sieved particles were introduced in a U-shaped fixed bed quartz reactor. It was reduced *in situ* with H_2 (30 mL min^{-1}) for 1 h at 800 °C and then purged with N_2.

Then, the reactor was fed with a gas mixture consisting of CH_4 and CO_2 (molar ratio 1:1) diluted in Ar corresponding to a Gas Hourly Space Velocity (GHSV) of 60,000 mL g^{-1} h^{-1}. The total flow was 100 mL min^{-1}. The gases were analyzed at 50 °C intervals starting at 400°C and ending at 800°C. At each temperature, ten injections were carried out in a Varian 3800 gas chromatograph. The products (H_2, CO_2, CO, and CH_4) are analyzed with a thermal conductivity detector (TCD) after separation on a molecular sieve (H_2 and CO) and a HayeSep Q column (CO_2 and CH_4).

The catalytic performances were evaluated by the conversions of CH_4 (X_{CH_4}) and CO_2 (X_{CO_2}), the selectivities of H_2 (S_{H_2}) and CO (S_{CO}), to obtain their ratio and carbon balance (CB), which were calculated as follows:

- Methane Conversion (X_{CH4}):

$$X_{CH_4} = \frac{(n_{CH_4,in} - n_{CH_4,out})}{n_{CH_4,in}} \times 100 \quad (3)$$

- Carbon dioxide Conversion (X_{CO2})

$$X_{CO_2} = \frac{(n_{CO_2,in} - n_{CO_2,out})}{n_{CO_2,in}} \times 100 \quad (4)$$

- Selectivity of Hydrogen (S_{H2})

$$S_{H_2} = \frac{n_{H_2,out}}{2(n_{CH_4,in} - n_{CH_4,out})} \times 100 \quad (5)$$

- Selectivity of carbon monoxide (S_{CO})

$$S_{CO} = \frac{n_{CO,out}}{(n_{CH_4,in} + n_{CO_2,in}) - (n_{CH_4,out} + n_{CO_2,out})} \times 100 \quad (6)$$

- H_2/CO Ratio

$$\text{Ratio } H_2/CO = \frac{S_{H_2}}{S_{CO}} \quad (7)$$

- Carbon balance

$$CB = \frac{n_{CO_2,out} + n_{CH_4,out} + n_{CO,out}}{n_{CH_4,in} + n_{CO_2,in}} \times 100 \quad (8)$$

3. Results and discussion

The X-ray diffraction (XRD) patterns of the powders calcined at 700 ºC are shown in Fig. 1. The pattern obtained for the reference Ni-CGO sample (Fig. 1 (a)) shows the expected diffraction peaks for the rocksalt-type NiO and the fluorite-type $Ce_{0.9}Gd_{0.1}O_{1.95}$ (CGO) phases, both corresponding to the cubic structure (*Fm-3m* space group), indicating the effectiveness of the one-step synthesis route on the preparation of composite mixtures.

In contrast, in the case of the patterns obtained for both the Co- (Fig. 1 ((b) and (c)) and the Cu-containing samples (Fig. 1 (d) and (e)), the XRD patterns show the presence of a mixture of different oxides. In both sets of samples, we can observe peaks belonging to the (Ni,Co)O and to the (Ni,Cu)O solid solutions, which is confirmed by the slight peak shifting from the reference Ni-CGO sample. Nonetheless, additional peaks belonging to the spinel-type Co_3O_4 (JCPDS file nº 43-1003) and the tenorite-type CuO (JCPDS file nº 78-0428) phases can also be found. In addition, the phase abundancy determined by Ritveld refinement for these phases increase with increasing dopant content (Table 2). This behavior can be explained by the relatively low solubility limit of both Co and Cu oxides into NiO lattice, as previously reported in the phase equilibrium diagrams for these oxide systems [32,33].

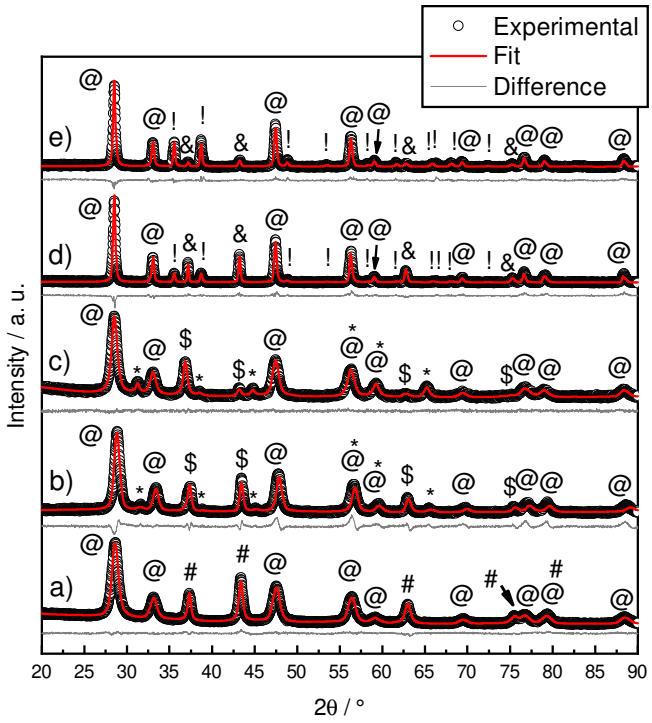

Fig. 1 – X-ray diffraction patterns of the powders calcined at 700 ºC: a) Ni-CGO, b) $Ni_{0.6}Co_{0.4}$-CGO, c) $Ni_{0.2}Co_{0.8}$-CGO, d) $Ni_{0.6}Cu_{0.4}$-CGO, e) $Ni_{0.2}Cu_{0.8}$-CGO. @ - CGO; # - NiO; $ - (Ni,Co)O; & - (Ni,Cu)O; * - Co_3O_4; ! - CuO.

Table 2 – Crystallographic parameters, phase abundancy and refined indices for all samples upon calcination, evaluated by Rietveld refinement.

Sample	Phase	Lattice parameter / Å			Phase abundancy / %	R_{wp} / %	χ^2
		a	*b*	*c*			
Ni-CGO	**NiO**	2.9537(2)	2.9537(2)	7.2410(1)	47.88	1.53	2.03
	CGO	5.4167(7)	5.4167(7)	5.4167(7)	52.12		
$Ni_{0.6}Co_{0.4}$-CGO	**(Ni,Co)O**	2.9516(4)	2.9516(4)	7.2391(12)	34.78	2.81	8.14
	Co_3O_4	8.0516(9)	8.0516(9)	8.0516(9)	16.66		
	CGO	5.3873(6)	5.3873(6)	5.3873(6)	48.56		
$Ni_{0.2}Co_{0.8}$-CGO	**(Ni,Co)O**	2.9531(8)	2.9531(8)	7.2904(5)	7.26	1.10	1.31
	Co_3O_4	8.0915(7)	8.0915(7)	8.0915(7)	44.95		
	CGO	5.4161(3)	5.4161(3)	5.4161(3)	47.79		
$Ni_{0.6}Cu_{0.4}$-CGO	**(Ni,Cu)O**	2.9603(8)	2.9603(8)	7.2566(8)	33.47	10.06	2.37
	CuO	4.6966(7)	3.4309(9)	5.1184(3)	11.18		
	CGO	5.4191(4)	5.4191(4)	5.4191(4)	53.36		
$Ni_{0.2}Cu_{0.8}$-CGO	**(Ni,Cu)O**	2.9561(3)	2.9561(3)	7.2444(1)	9.14	9.23	2.38
	CuO	4.6825(2)	3.4238(7)	5.1192(2)	31.85		
	CGO	2.9603(8)	2.9603(8)	7.2566(8)	59.00		

This noted coexistence of different oxide phases can be explained based on the stability diagrams of oxygen partial pressure (p_{O2}) *vs.* temperature, calculated by thermodynamic calculations [34]. Calculations were performed using the *FactSage* thermochemical software, in the module stability diagrams, which accounts for the equilibrium constants of each reaction to establish a correlation with each p_{O2} [34]. Fig. 2 depicts the obtained solutions for the Ni-, Cu- and Co-containing systems. We can observe that the conditions used in the calcination step (in air, p_{O2} ~ 0.21 atm), in the case of the Co-containing samples, Co_2O_3 is the most stable phase in the whole temperature range. However, in the case of the Ni- and Cu-based systems, both NiO and CuO are, respectively, the most stable phases. Conversely, the metallic forms of each composition are only stable under very low p_{O2} values in all cases.

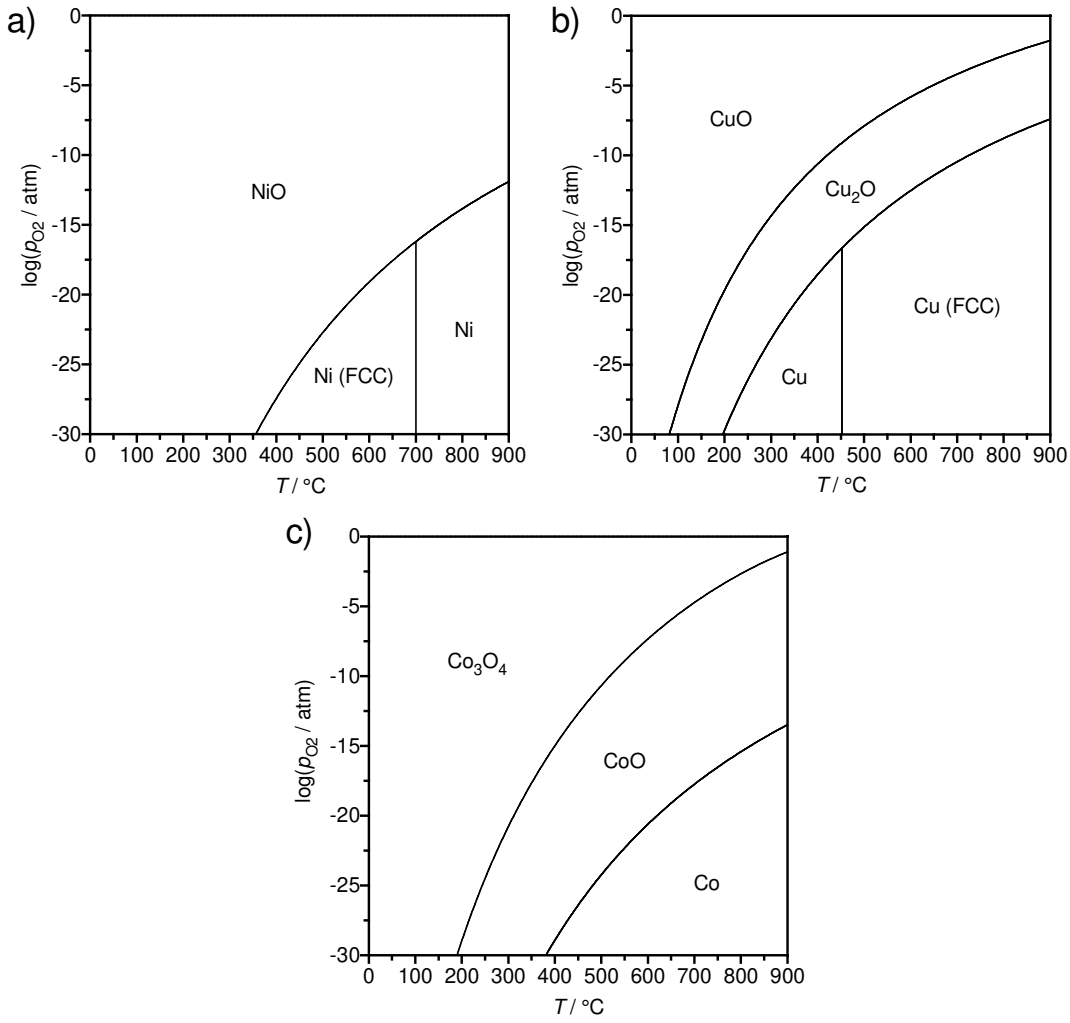

Fig. 2 – Stability diagrams of a) Ni, b) Cu, and c) Co systems, obtained from thermodynamic calculations of the oxygen partial pressure (p_{O2}) as a function of temperature [34].

Table 3 – Specific surface area and H_2 consumption of the samples.

Property	Specific surface area / m^2 g^{-1}	H_2 consumption / µmol g^{-1}	
Sample	Calcined	Calcined	Theoretical
Ni-CGO	21	8012	8519
$Ni_{0.6}Co_{0.4}$-CGO	17	7943	8505
$Ni_{0.2}Co_{0.8}$-CGO	19	10010	8491
$Ni_{0.6}Cu_{0.4}$-CGO	11	7325	8246
$Ni_{0.2}Cu_{0.8}$-CGO	10	7772	7990

The H_2-TPR analyses, shown in Fig. 3, were performed to assess the reducibility of the newly synthesized anode powders. The CGO matrix shows no reduction peaks under the measured experimental conditions, agreeing with previous reports [35]. In contrast, the Ni-CGO sample exhibits a wide overlapped peak at around 346 °C, which can be related to the reduction of the surface and/or surface-bulk of the NiO species into metallic nickel, according to [36]:

$$NiO + H_2 \rightarrow Ni^0 + H_2O \quad (9)$$

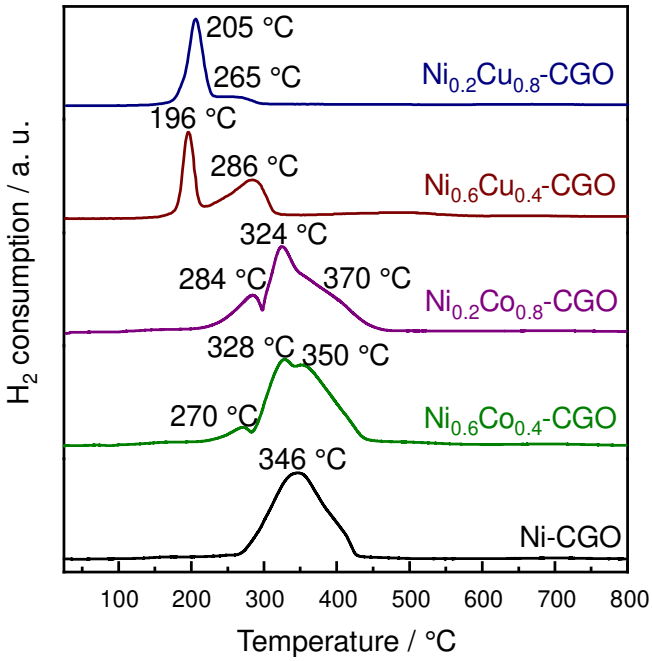

Fig. 3 – Hydrogen Temperature-programmed reduction (H_2-TPR) profiles of the samples.

As shown in Fig. 3, the NiCo-based powders have one well-defined peak at low temperature (284 or 270 °C) attributed to the stepwise overall reduction of Co_3O_4 (Eq. 10) [37,38]. The reduction at higher temperatures (300-400 ºC) can be attributed to the simultaneous reduction of Co^{2+} species to metallic Co^0 (Eq. 11) and Ni^{+2} to Niº (Eq. 9). Besides, an increase in the peak area and a slight shift of the NiCo peaks towards higher temperatures has been observed as the Co content increases.

$$Co_3O_4 + H_2 \rightarrow 3CoO + H_2O \quad (10)$$

$$CoO(s) + H_2(g) \rightarrow Co^0(s) + H_2O(g) \quad (11)$$

According to Fig. 3, the NiCu-based sample exhibits large asymmetric peaks in the temperature range 195 – 205 °C, which may be attributed to the CuO reduction to metal copper (Cu^0), as shown in (Eq. 12) [35,39]. As expected, H_2 consumption is proportional to the Cu content (Table 2). The addition of Cu to the Ni-based powder leads to a shift in the reduction profiles of the NiCGO to a comparatively lower temperature (265 °C, 286 °C).

$$CuO(s) + H_2(g) \rightarrow Cu^0(s) + H_2O(g) \quad (12)$$

The reduction sequence of both Co- and Cu-containing samples agrees with that predicted in the stability diagrams of Fig. 2, due to the decreased oxygen partial pressure in H_2 atmosphere. Furthermore, the XRD patterns confirm that after reduction, all samples exhibit the presence of the CGO phase with (mono/bi)-active metallic phases.

By comparing the Co- and the Cu-promoted Ni samples, we can observe that the reduction peaks are shifted towards higher temperatures with the addition of Co, while in the case of Cu-containing samples, the peaks are shifted towards lower temperatures. The noted shift towards higher temperatures in the case of the Co-containing samples can be directly related to the increased metal-support interactions [40], in comparison to those from NiCGO and Cu-containing samples. However, the intimate contact between the metallic and the ceramic phases is crucial to facilitate the hydrogen spillover [40]. TEM analysis of both $Ni_{0.2}Co_{0.8}$-CGO and $Ni_{0.2}Cu_{0.8}$-CGO samples are depicted in Fig. 4 as an example, exhibiting mean particle sizes of 23.87 and 15.46 nm, respectively.

The total H_2 consumption of NiCo and NiCu samples is shown in Table 3, where higher values were found for the Co-containing samples. Importantly, the estimated value of H_2 consumption determined for the $Ni_{0.2}Co_{0.8}$-CGO sample is substantially higher than that of the theoretical value (Table 3). Similar observations have been reported for NiCu-based compositions in the work of Bonura *et al.* [35], where the authors have described this effect to be related to the reduction of copper. Hence, in the $Ni_{0.2}Co_{0.8}$-CGO sample, cobalt reduction would possibly favor the hydrogen spillover, thus, leading to the increased value of H_2 consumption in the $Ni_{0.2}Co_{0.8}$-CGO sample. Moreover, this phenomenon may also be interfering with the H_2 consumption values among the remaining samples.

In addition, Co-containing samples have a higher surface area than Cu-containing samples (Table 2), which may allow greater accessibility to the gases at their surface and therefore also expected to benefit the catalytic activity of these compositions.

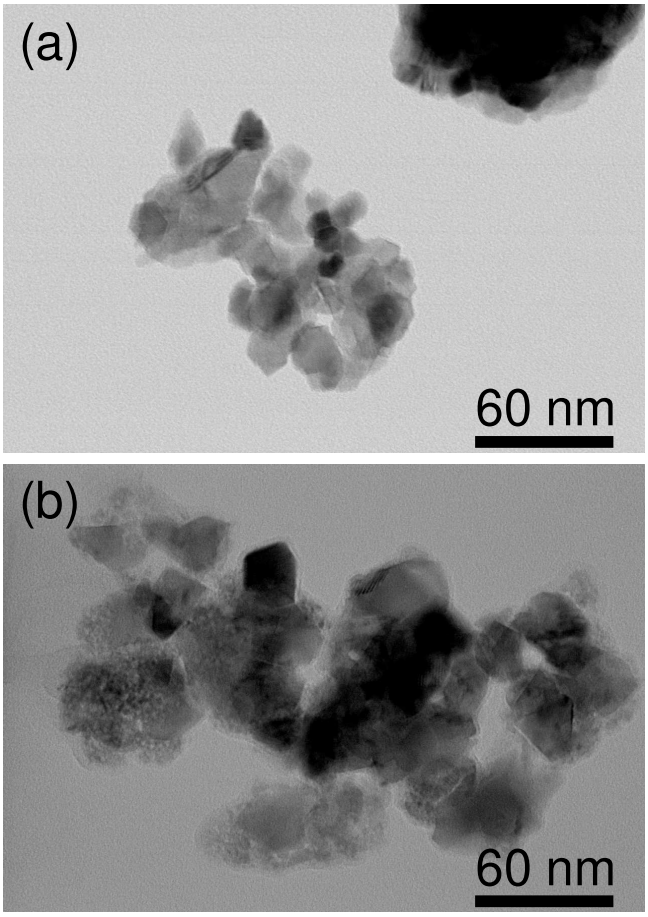

Fig. 4 – TEM image of the (a) $Ni_{0.2}Cu_{0.8}$-CGO and (b) $Ni_{0.2}Co_{0.8}$-CGO powders upon reduction.

The XRD of the reduced samples is depicted in Fig. 5. From this figure, we can observe the main peaks related to the CGO structure in all cases. After reduction, CGO sample showed only CGO peaks (XRD pattern not shown), which justifies that the sample was not reduced and corroborates with the TPR analysis. In the case of the reduced Co-containing samples ($Ni_{0.6}Co_{0.4}$-CGO and $Ni_{0.2}Co_{0.8}$-CGO), the patterns reveal the presence of the NiCo reflections, with minor peaks belonging to the remaining traces of CoO. This behavior contrasts with that

observed for the XRD patterns of the calcined powders, where a mixture of different oxides was observed. However, it is interesting to note that in the XRD from the calcined powders, the formation of complete solid solubility can be noted in the case of the Co-containing catalysts, in agreement with the phase equilibrium diagram for the NiCo alloys [41].

Interestingly, in the NiCu solid solutions, a clear separation into two peaks can be observed. These peaks are close to the standard positions for the pure metals, *e.g.*, for the Cu (111) and Ni (111) reflections of the face-centered cubic (fcc) structure. However, we can note that significant peak shifting from the relative positions of the pure metals occurs, indicating the formation of some solid solution in these two end members. The presence of two diffusion couples is well reported for this system [17,42,43], and it relates to the formation of two NiCu-based solid solutions (*e.g.*, α_1: Cu-rich and α_2: Ni-rich), both with a limited solid solubility range. As expected, the relative intensity of the Cu-rich peak increases for the $Ni_{0.2}Cu_{0.8}$-CGO catalyst, while the Ni-rich peak decreases. In addition, small peaks corresponding to CoO and Cu_2O phases are also detected, as a likely result of an incomplete reduction and/or changes in the equilibrium during cooling (Fig. 2). Nonetheless, the content of the remaining oxidized phases is only around 5 wt%, thus, possible disappearing during the DRM measurements.

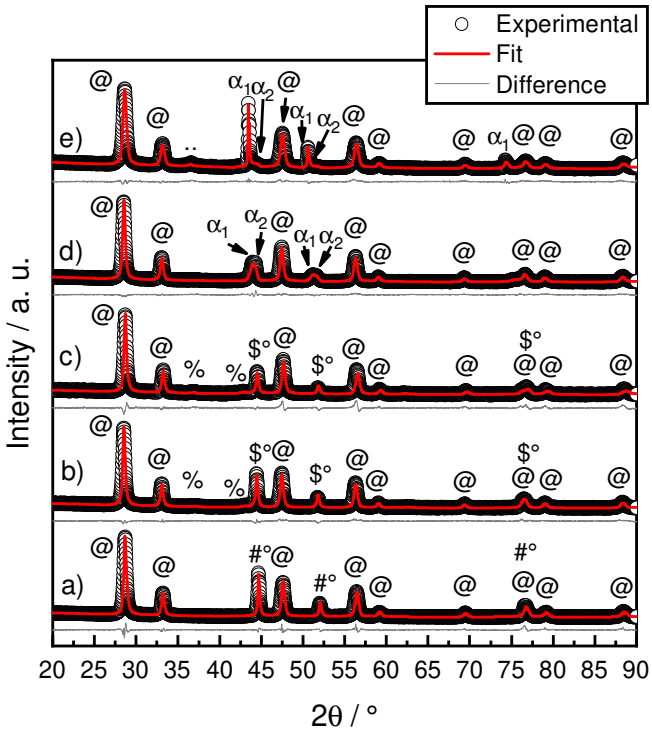

Fig. 5 – X-ray diffraction patterns of the reduced samples: a) Ni-CGO, b) $Ni_{0.6}Co_{0.4}$-CGO, c) $Ni_{0.2}Co_{0.8}$-CGO, d) $Ni_{0.6}Cu_{0.4}$-CGO, e) $Ni_{0.2}Cu_{0.8}$-CGO. @ - CGO; #° - Ni; $° - Ni-Co; % - CoO; ¨ - Cu_2O; α_1 - Cu-rich Ni-Cu; α_2 - Ni-rich Ni-Cu.

Table 4 – Crystallographic parameters, phase abundancy and refined indices for all samples upon reduction, evaluated by Rietveld refinement.

Sample	Phase	Lattice parameter / Å			Phase abundancy / %	R_{wp} / %	χ^2
		a	*b*	*c*			
Ni-CGO	**Ni**	3.5140(5)	3.5140(5)	3.5140(5)	40.76	2.60	5.64
	CGO	5.4119(9)	5.4119(9)	5.4119(9)	59.24		
$Ni_{0.6}Co_{0.4}$-CGO	**(Ni,Co)**	3.5278(2)	3.5278(2)	3.5278(2)	37.40	1.45	2.12
	CoO	4.2033(1)	4.2033(1)	4.2033(1)	5.65		
	CGO	5.4181(1)	5.4181(1)	5.4181(1)	56.96		
$Ni_{0.2}Co_{0.8}$-CGO	**(Ni,Co)**	3.5327(9)	3.5327(9)	3.5327(9)	30.34	2.01	4.63
	CoO	4.2134(1)	4.2134(1)	4.2134(1)	6.03		
	CGO	5.4032(1)	5.4032(1)	5.4032(1)	63.63		
$Ni_{0.6}Cu_{0.4}$-CGO	**α_1 (Cu-rich)**	3.5682(9)	3.5682(9)	3.5682(9)	11.07	1.96	2.99
	α_2 (Ni-rich)	3.5456(7)	3.5456(7)	3.5456(7)	26.28		
	CGO	5.4190(2)	5.4190(2)	5.4190(2)	62.65		
$Ni_{0.2}Cu_{0.8}$-CGO	**α_1 (Cu-rich)**	3.6110(6)	3.6110(6)	3.6110(6)	25.69	2.23	3.36
	α_2 (Ni-rich)	3.5497(4)	3.5497(4)	3.5497(4)	7.62		
	Cu_2O	4.2611(4)	4.2611(4)	4.2611(4)	4.83		
	CGO	5.4198(6)	5.4198(6)	5.4198(6)	61.86		

Fig. 6 and 7 show the CH_4 and CO_2 conversions, H_2 and CO selectivity, H_2 and CO yield, carbon balance, and C_2H_4 concentration during the DRM reaction from 400 to 800 °C.

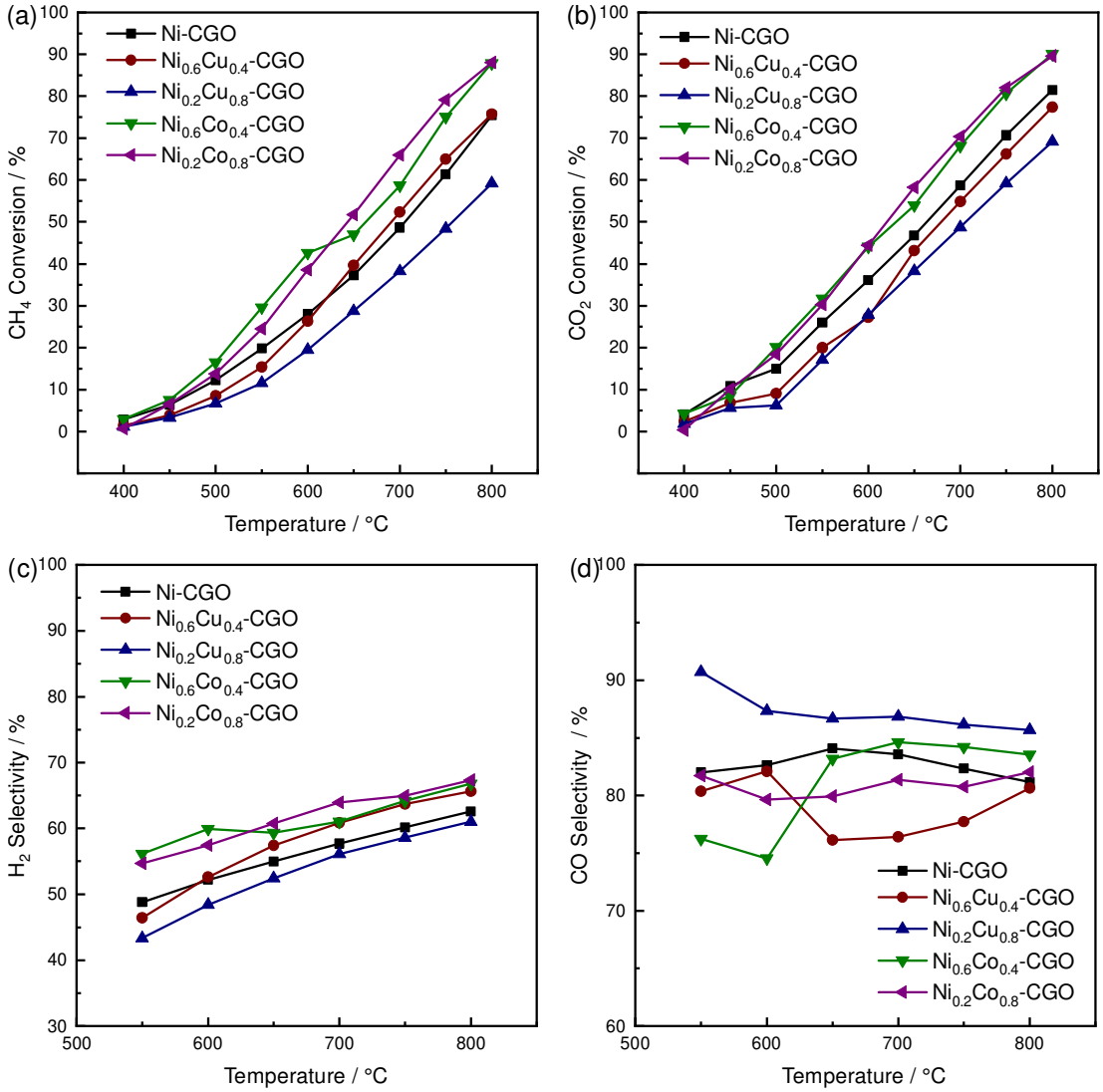

Fig. 6 – (a) CH_4 conversion, (b) CO_2 conversion, (c) H_2 selectivity, and (d) CO selectivity obtained during the DRM reaction over the different samples.

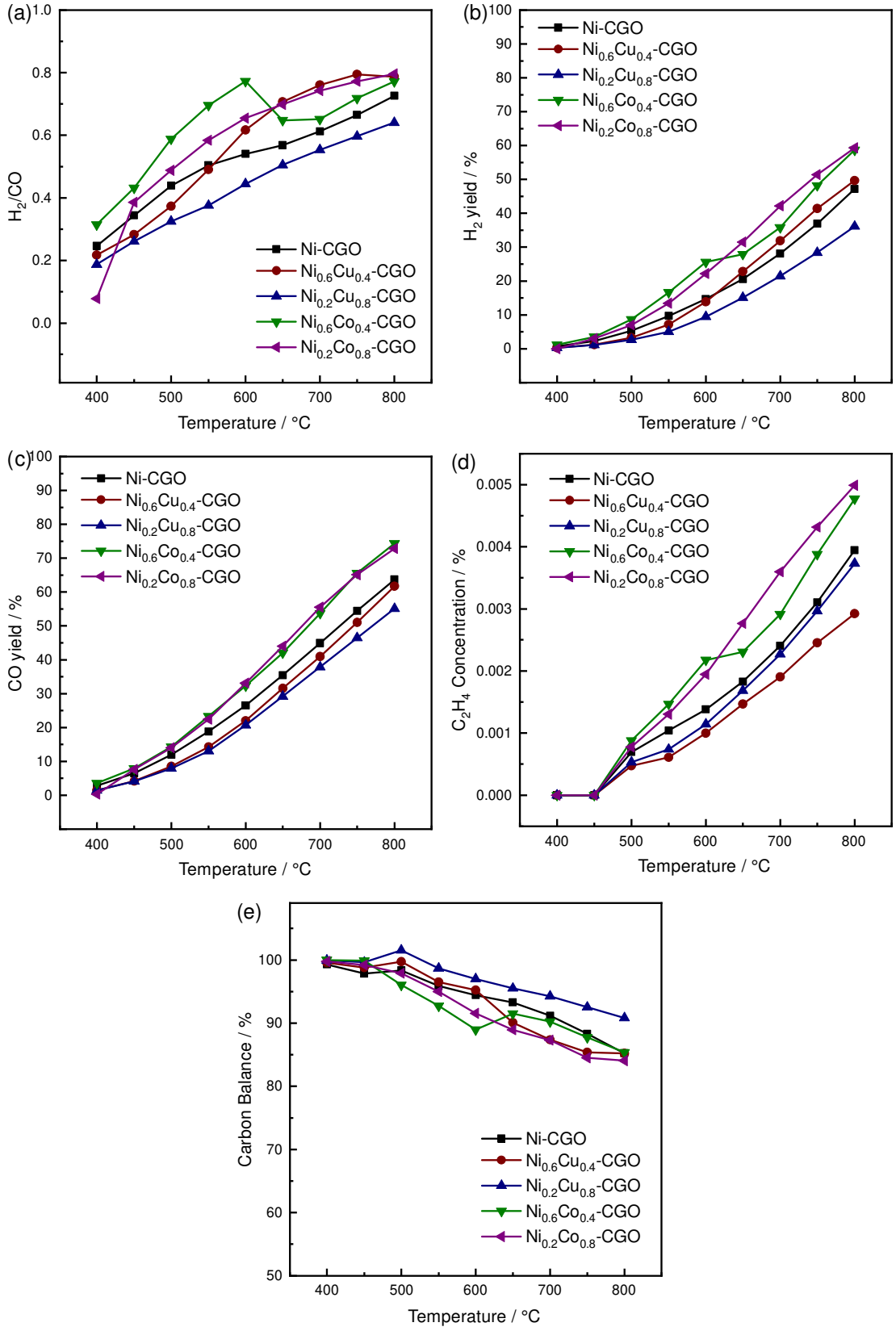

Fig. 7 – (a) H_2/CO ratio, (b) H_2 yield, (c) CO yield, (d) C_2H_4 concentration, and (e) carbon balance obtained during the DRM reaction over the different samples.

The CH_4 and CO_2 conversions increased with the reaction temperature due to the endothermic character of the DRM reaction [6]. Furthermore, since stoichiometric amounts of CH_4 and CO_2 were used, the conversions of CH_4 and CO_2 should be equal, and, according to Eq. (1), the H_2/CO ratio should be unity at all temperatures. Fig. 7 (a) indicates that the H_2/CO ratio is not equal to 1. Such a result confirms the occurrence of secondary reactions, from which trace amounts of ethylene (C_2H_4) were detected (0.005%).

The discrepancies with typical thermodynamic predictions are due to secondary reactions that occur simultaneously with DRM. These unfavorable reactions, Eqs. (13)-(18), have a strong influence on the performance of the DRM reaction and contribute to the reactants or products consumption without being strictly accounted for the equilibrium calculation.

The results further indicate that the Reverse Water Gas Shift (RWGS) and methanation reactions, Eqs. (13) and (14), contribute to an increase in the conversion of CO_2 and a decrease in the H_2 selectivity.

However, the occurrence of the Boudouard reaction, Eq. (15), the reverse of carbon gasification (Eq. (16)), and the methane decomposition Eq. (17) and non-oxidative methane coupling (18) reactions are also possible.

Reverse Water Gas Shift reaction (favorable > 600 °C):

$$CO_2 + H_2 \rightarrow CO + H_2O \quad (13)$$

Methanation (favorable < 750 ºC):

$$CO_2 + 4\,H_2 \rightarrow CH_4 + 2\,H_2O \quad (14)$$

Boudouard reaction (favorable < 750 ºC):

$$2\,CO \rightarrow C + CO_2 \quad (15)$$

Reverse of carbon gasification (favorable < 750 ºC):

$$CO + H_2 \rightarrow C + H_2O \quad (16)$$

Methane decomposition (favorable > 500 ºC):

$$CH_4 \rightarrow C + 2\,H_2 \quad (17)$$

Non-oxidative methane coupling:

$$2\,CH_4 \rightarrow 2\,H_2 + C_2H_4 \quad (18)$$

According to Fig. 6 ((a) and (b)), the NiCo-based samples showed higher CH_4 and CO_2 conversions among all the samples. The NiCo-based samples exhibited higher H_2/CO ratios than NiCu-based and Ni-CGO samples in the range temperature of 400 to 650 °C (Fig. 7 (a)).

Before 600 °C, the $Ni_{0.6}Co_{0.4}$-CGO sample has a higher H_2/CO ratio than that of $Ni_{0.2}Co_{0.8}$-CGO, which can be related to its higher activity in the methane decomposition reaction (Eq. (17)). Hence, this contribution to product distribution would cause an increase in H_2 production as well as carbon formation in accordance with the carbon balance Fig. 7 (e). The occurrence of the Boudouard reaction (Eq. (15)) cannot be excluded.

The strong decrease in H_2/CO ratio (Fig. 7 (a)) after 600 °C may be related to the RWGS reaction (Eq. (13)) that is favored at high temperatures. The increase in CO selectivity confirms this hypothesis (Fig. 6 (d)).

Regarding the H_2 selectivity (Fig. 6 (c)) and H_2 yield (Fig. 7 (b)) the NiCo-based samples are shown to be the most promising materials at all temperatures.

Co-promoted catalysts are the more active compositions among the tested samples. The synergy between Ni and Co particles has been highlighted as the reason for the better performance of these samples, as discussed in previous studies [44,45]. In addition, Co-promoted Ni samples showed strong metal-ceramic interaction (confirmed by TPR) and formation of Ni-Co stable solid solutions (as confirmed by XRD). The formation of the NiCo alloy can promote high

reducibility, particularly in the $Ni_{0.2}Co_{0.8}$-CGO sample. All these factors are important to avoid active phase sintering and carbon deposition, improving the catalytic properties and longevity [25,46–48]. This behavior is concomitant with the estimated larger surface area in the case of the Co-containing samples (Table 2). Therefore, the dry reforming of methane reaction appears to be more favored in the presence of $Ni_{0.2}Co_{0.8}$-CGO.

Fig. 7 (e) shows the carbon balance over the catalysts. At 400 and 450 °C, the carbon balance is close to 100% because the samples exhibited low conversions. Carbon balance lower than 100 % implies that part of the carbon atoms, which are not present in the outgoing gas, are instead deposited on the samples' surface in the form of carbon deposits [6].

The $Ni_{0.6}Co_{0.4}$-CGO sample showed a decrease in the carbon balance, reaching a minimum at 600 °C and then a slight increase at 650 °C. Ni-CGO and $Ni_{0.2}Cu_{0.8}$-CGO samples showed values of carbon balance relatively higher than those noted for the NiCo-based and $Ni_{0.6}Cu_{0.4}$-CGO samples due to their lower activities. The amount of carbon produced during the DRM reaction was evaluated by the TG/DSC profiles shown in Fig. 8.

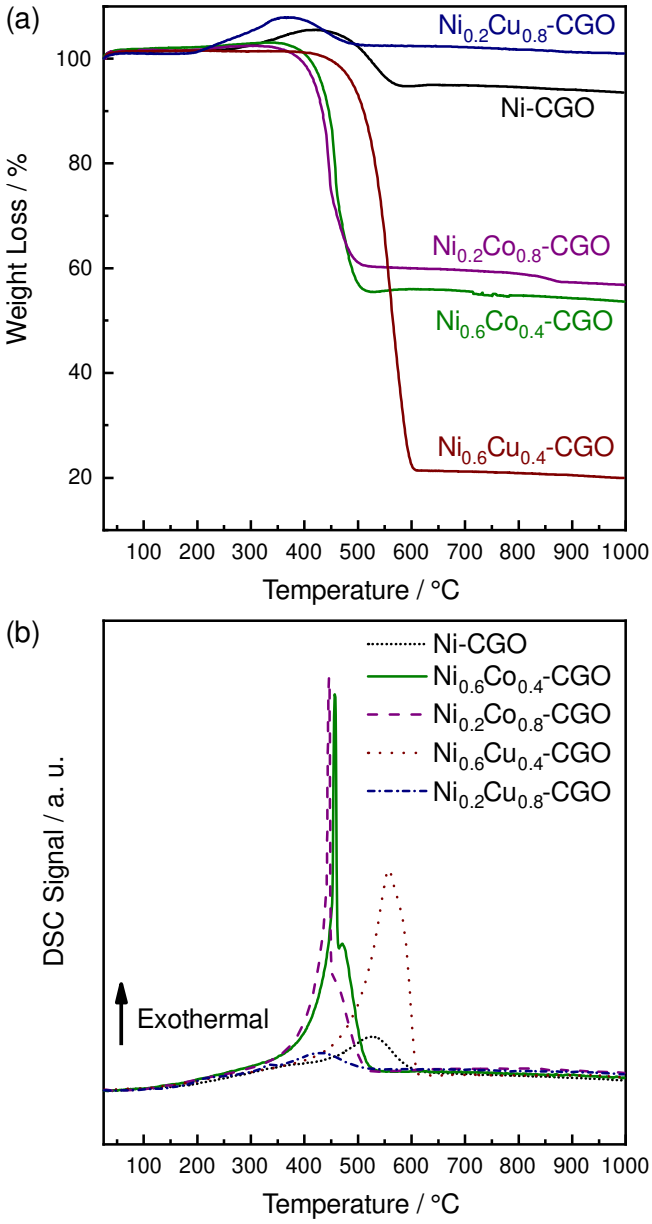

Fig. 8 – TG (a) DSC (b) profiles obtained after oxidation in air of the catalysts upon DRM reaction.

The Ni-CGO and $Ni_{0.2}Cu_{0.8}$-CGO samples have shown only a slight weight gain (5-8%) between 200 and 400 °C (Fig. 8a) due to the uptake of oxygen by metallic nickel present in the samples after the catalytic tests ($Ni^0 + 1/2O_2 \rightarrow NiO$). However, all samples presented weight loss at 400 - 600 °C and exothermic phenomena, which are attributed to carbon oxidation ($O_2 + C_{adsorbed} \rightarrow CO_2$) [49].

The following order is described for weight losses (%): $Ni_{0.6}Cu_{0.4}$-CGO (77.8%) > $Ni_{0.6}Co_{0.4}$-CGO (47.5%) ≈ $Ni_{0.2}Co_{0.8}$-CGO (42.1%) > Ni-CGO (10.8%) > $Ni_{0.2}Cu_{0.8}$-CGO (5.3%).

$Ni_{0.6}Cu_{0.4}$-CGO has higher carbon deposition than that observed for the NiCo-based samples, as confirmed by XRD (Fig. 9). On the other hand, both Ni-CGO and $Ni_{0.2}Cu_{0.8}$-CGO samples showed lower carbon deposition than the NiCo-based and $Ni_{0.6}Cu_{0.4}$-CGO samples due to their low activities in dry reforming of methane according to the carbon balance results.

According to Fig. 8 (b), non-symmetrical exothermic phenomena are observed, indicating different oxidation peaks corresponding to different carbonaceous species on the samples' surface, except for the Ni-CGO sample. NiCo sample showed a lower temperature of the exothermic phenomenon compared to the $Ni_{0.6}Cu_{0.4}$-CGO sample. As expected, the Ni-CGO and $Ni_{0.2}Co_{0.8}$-CGO samples showed low intensity peaks in the exotermic phenomenon, according to their reactivities. Co-containing samples showed narrow peaks with a relatively high intensity between 440-470 ºC that can be attributed to the oxidation of adsorbed carbon species forming complexes with the metallic surface species. While the peak (550-570 ºC) corresponding to the $Ni_{0.6}Cu_{0.4}$-CGO catalyst may be related to C_β. C_β species may be responsible for the lower efficiency of the sample, as it is in the proximity of catalytic sites, making it less accessible to gaseous reagents [31].

The stronger interaction between Ni and Co metals (confirmed by TPR) provides a better carbon resistance on the surface of the catalyst. The Co-containing samples showed a higher reduction temperature, which is related to strong metal-ceramic interactions. This intimate NiCo metal-ceramic contact allowed better CO_2 adsorption on the ceramic, which is beneficial for limiting the rate of carbon deposition. Therefore, the NiCo-based samples are demonstrated as promising anode materials to enhance the adsorption of CO_2 in the ceria–gadolinia matrix, which reduces the formation of carbon through the reverse Boudouard reaction ($CO_2 + C \rightleftharpoons 2CO$). This effect has been more pronounced for the $Ni_{0.2}Co_{0.8}$-CGO sample.

The XRD patterns of the spent catalysts are shown in Fig. 9. The *Rietveld* refined crystallographic parameters and phase abundancy are given in Table 5.

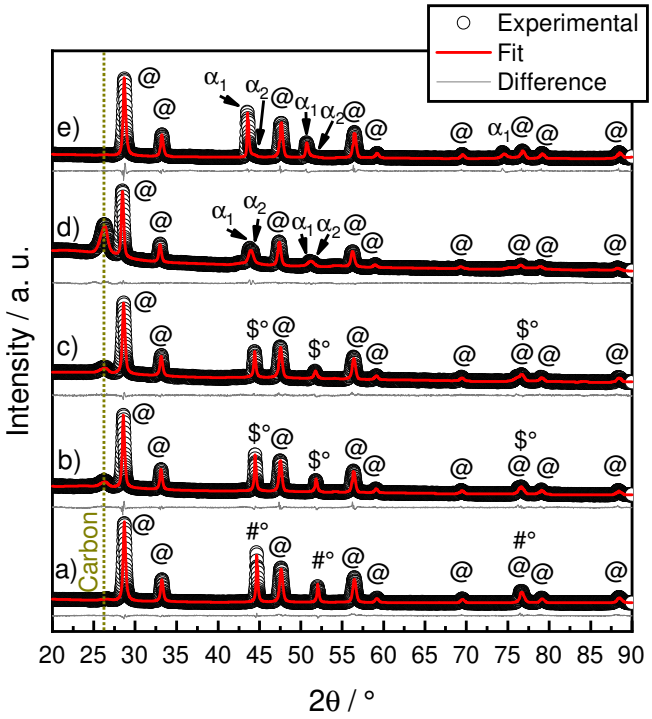

Fig. 9 – XRD patterns of the catalysts upon DRM: a) Ni-CGO, b) $Ni_{0.6}Co_{0.4}$-CGO, c) $Ni_{0.2}Co_{0.8}$-CGO, d) $Ni_{0.6}Cu_{0.4}$-CGO, e) $Ni_{0.2}Cu_{0.8}$-CGO. @ - CGO; #° - Ni; $° - Ni-Co; α_1 - Cu-rich Ni-Cu; α_2 - Ni-rich Ni-Cu.

Table 5 – Crystallographic parameters, phase abundancy and refined indices for all samples upon DRM reaction, evaluated by Rietveld refinement.

Sample	Phase	Lattice parameter / Å			Phase abundancy / %	R_{wp} / %	χ^2
		a	*b*	*c*			
Ni-CGO	**Ni**	3.5232(8)	3.5232(8)	3.5232(8)	36.46	1.97	3.19
	CGO	5.4212(3)	5.4212(3)	5.4212(3)	50.37		
	C	2.4970(1)	2.4970(1)	6.7716(5)	13.17		
$Ni_{0.6}Co_{0.4}$-CGO	**(Ni,Co)**	3.5225(5)	3.5225(5)	3.5225(5)	31.15	1.98	3.88
	CGO	5.4119(8)	5.4119(8)	5.4119(8)	42.77		
	C	2.4249(2)	2.4249(2)	6.7522(2)	26.08		
$Ni_{0.2}Co_{0.8}$-CGO	**(Ni,Co)**	3.5344(1)	3.5344(1)	3.5344(1)	25.71	1.36	1.98
	CGO	5.4187(2)	5.4187(2)	5.4187(2)	46.80		
	C	2.5020(4)	2.5020(4)	6.7820(1)	27.49		
$Ni_{0.6}Cu_{0.4}$-CGO	**α_1 (Cu-rich)**	3.5781(8)	3.5781(8)	3.5781(8)	4.86	2.19	3.16
	α_2 (Ni-rich)	3.5633(1)	3.5633(1)	3.5633(1)	5.72		
	CGO	5.4189(6)	5.4189(6)	5.4189(6)	14.41		
	C	2.4570(6)	2.4570(6)	6.7482(1)	75.01		
$Ni_{0.2}Cu_{0.8}$-CGO	**α_1 (Cu-rich)**	3.6018(7)	3.6018(7)	3.6018(7)	32.33	3.05	6.37
	α_2 (Ni-rich)	3.5392(3)	3.5392(3)	3.5392(3)	3.64		
	CGO	5.4132(1)	5.4132(1)	5.4132(1)	60.67		
	C	2.4916(7)	2.4916(7)	6.7582(8)	3.36		

All samples exhibit nearly identical characteristic diffraction peaks to those presented by the reduced samples (Fig. 5), indicating that phase composition remains effectively stable after the catalytic tests, as also confirmed by *Rietveld* refinement (Table 5). In addition, the small peaks of the remaining Cu_2O and CoO phases are not detected, indicating that complete reduction has occurred during the DRM reaction, as expected due to the very low p_{O2} typical for these environments [17]. Nonetheless, the post-reaction Ni-CGO and Co-based samples contain a rhombohedral (29123-ICSD, a = 3.635 Å, alpha = 39.82°) carbon phase (Fig. 9).

The XRD patterns of the $Ni_{0.6}Cu_{0.4}$-CGO samples indicated the formation of the Ni-Cu alloy (JCPDS file nº 65-7246, a = 3.5615 Å) [35] after reduction and reactivity test (Fig. 9). *Rietveld* refinement data also confirmed the presence of this alloy (Table 5).

$Ni_{0.6}Cu_{0.4}$-CGO sample exhibited an intense rhombohedral carbon peak (around 75 wt%, Table 5), in good agreement with TG-DSC data, while a much lower carbon content of around 3 wt% was found for the $Ni_{0.2}Cu_{0.8}$-CGO sample (Table 5). Overall, the sequence agrees well with that determined by TG measurements (Fig. 8a).

Rietveld refinements for all samples confirm the crystal structure and lattice parameters of the phases agree with data from JCPDS and ICSD.

4. Conclusion

The one-step synthesis route was used to successfully synthesize cermet nanocrystalline powders made of Ni-, NiCo- and NiCu-based alloys and gadolinium-doped ceria. According to the TPR results, the Co-promoted Ni samples exhibited the highest surface area values, as determined from BET measurements, in addition to the highest reducibility and strongest metal-ceramic interaction among the tested materials. This behavior was shown to have a strong correlation to the increase of the catalytic activity observed for the Co-based catalysts, showing higher CH_4 and CO_2 conversions than those observed in the case of the Cu-based and Ni-CGO catalysts, as well as being able to mitigate the carbon deposition on the material's surface. The addition of cobalt to the Ni/CGO system appears to stabilize the active surface essentially by limiting the rate of coking to enhance the adsorption of CO_2 in the ceria–gadolinia phase, which reduces the formation of carbon through the reverse *Boudouard* reaction ($CO_2 + C \rightleftharpoons 2CO$). This work highlights the potential of this synthesis route in designing suitable anode compositions for the dry reforming of methane (DRM) reactions.

Acknowledgments

This study was financed in part by the Coordenação de Aperfeiçoamento de Pessoal de Nível Superior (CAPES/Brazil, Finance Code 001). Francisco J. A. Loureiro and Duncan P. Fagg acknowledge the projects PTDC/CTM-CTM/2156/2020, PTDC/QUI-ELT/3681/2020, POCI-01-0145-FEDER-032241, UIDB/00481/2020 and UIDP/00481/2020 - Fundação para a Ciência e a Tecnologia; and CENTRO-01-0145-FEDER-022083 - Centro Portugal Regional Operational Programme (Centro2020), under the PORTUGAL 2020 Partnership Agreement, through the European Regional Development Fund. Francisco J. A. Loureiro also acknowledges FCT for the financial support with the reference CEECIND/02797/2020. Allan Araújo thanks the Conselho

Nacional de Desenvolvimento Científico e Tecnológico (CNPq/Brazil, reference number 200439/2019-7).

References

[1] K. Ray, S. Sengupta, G. Deo, Reforming and cracking of CH_4 over Al_2O_3 supported Ni, Ni-Fe and Ni-Co catalysts, Fuel Process. Technol. 156 (2017) 195–203. https://doi.org/10.1016/j.fuproc.2016.11.003.

[2] C.A. Schwengber, F.A. Da Silva, R.A. Schaffner, N.R.C. Fernandes-Machado, R.J. Ferracin, V.R. Bach, H.J. Alves, Methane dry reforming using Ni/Al_2O_3 catalysts: Evaluation of the effects of temperature, space velocity and reaction time, J. Environ. Chem. Eng. 4 (2016) 3688–3695. https://doi.org/10.1016/j.jece.2016.07.001.

[3] A.V.P. Lino, E.M. Assaf, J.M. Assaf, Hydrotalcites derived catalysts for syngas production from biogas reforming: Effect of nickel and cerium load, Catal. Today. 289 (2017) 78–88. https://doi.org/10.1016/j.cattod.2016.08.022.

[4] Y. Wang, L. Yao, S. Wang, D. Mao, C. Hu, Low-temperature catalytic CO_2 dry reforming of methane on Ni-based catalysts: A review, Fuel Process. Technol. 169 (2018) 199–206. https://doi.org/10.1016/j.fuproc.2017.10.007.

[5] B. Abdullah, N.A. Abd Ghani, D.V.N. Vo, Recent advances in dry reforming of methane over Ni-based catalysts, J. Clean. Prod. 162 (2017) 170–185. https://doi.org/10.1016/j.jclepro.2017.05.176.

[6] C. Tanios, S. Bsaibes, C. Gennequin, M. Labaki, F. Cazier, S. Billet, H.L. Tidahy, B. Nsouli, A. Aboukaïs, E. Abi-Aad, Syngas production by the CO_2 reforming of CH_4 over Ni–Co–Mg–Al catalysts obtained from hydrotalcite precursors, Int. J. Hydrogen Energy. 42 (2017) 12818–12828. https://doi.org/10.1016/j.ijhydene.2017.01.120.

[7] F.J.A. Loureiro, D. Pérez-Coll, V.C.D. Graça, S.M. Mikhalev, A.F.G. Ribeiro, A.

Mendes, D.P. Fagg, Proton conductivity in yttrium-doped barium cerate in nominally dry reducing conditions for application in chemical synthesis, J. Mater. Chem. A. 7 (2019) 18135–18142. submitted.

[8] S.H. Morejudo, R. Zanón, S. Escolástico, I. Yuste-Tirados, H. Malerød-Fjeld, P.K. Vestre, W.G. Coors, A. Martínez, T. Norby, J.M. Serra, C. Kjølseth, Direct conversion of methane to aromatics in a catalytic co-ionic membrane reactor, Science (80-.). 353 (2016) 563 LP – 566. http://science.sciencemag.org/content/353/6299/563.abstract.

[9] W. Wang, C. Su, Y. Wu, R. Ran, Z. Shao, Progress in Solid Oxide Fuel Cells with Nickel-Based Anodes Operating on Methane and Related Fuels, Chem. Rev. 113 (2013) 8104–8151. https://doi.org/10.1021/cr300491e.

[10] B. Chen, H. Xu, Y. Zhang, F. Dong, P. Tan, T. Zhao, M. Ni, Combined methane reforming by carbon dioxide and steam in proton conducting solid oxide fuel cells for syngas/power co-generation, Int. J. Hydrogen Energy. 44 (2019) 15313–15321. https://doi.org/https://doi.org/10.1016/j.ijhydene.2019.02.244.

[11] A.J.M. Araújo, J.P.F. Grilo, F.J.A. Loureiro, L.I.V. Holz, D.A. Macedo, D.P. Fagg, C.A. Paskocimas, Proteic sol–gel synthesis of Gd-doped ceria: a comprehensive structural, chemical, microstructural and electrical analysis, J. Mater. Sci. 55 (2020) 16864–16878. https://doi.org/10.1007/s10853-020-05173-6.

[12] S.J. Skinner, J.A. Kilner, Ion Conductors, Mater. Today. 6 (2003) 30–37.

[13] H. Inaba, H. Tagawa, Ceria-based solid electrolytes, Solid State Ionics. 83 (1996) 1–16. https://doi.org/https://doi.org/10.1016/0167-2738(95)00229-4.

[14] A. Lanzini, P. Leone, Experimental investigation of direct internal reforming of biogas in solid oxide fuel cells, Int. J. Hydrogen Energy. 35 (2010) 2463–2476. https://doi.org/https://doi.org/10.1016/j.ijhydene.2009.12.146.

[15] I. V Yentekakis, T. Papadam, G. Goula, Electricity production from wastewater treatment via a novel biogas-SOFC aided process, Solid State Ionics. 179 (2008) 1521–1525. https://doi.org/https://doi.org/10.1016/j.ssi.2007.12.049.

[16] S.A. Saadabadi, B. Illathukandy, P.V. Aravind, Direct internal methane reforming in biogas fuelled solid oxide fuel cell; the influence of operating parameters, Energy Sci. Eng. n/a (2021). https://doi.org/https://doi.org/10.1002/ese3.887.

[17] F.J.A. Loureiro, G.S. Souza, V.C.D. Graça, A.J.M. Araújo, P.F. Grilo, D.A. Macedo, D.P. Fagg, Nickel-copper based anodes for solid oxide fuel cells running on hydrogen and biogas: Study using ceria-based electrolytes with electronic short-circuiting correction, J. Power Sources. 438 (2019) 227041–227049. https://doi.org/10.1016/j.jpowsour.2019.227041.

[18] A.R.O. Sousa, A.J.M. Araujo, G.S. Souza, J.P.F. Grilo, F.J.A. Loureiro, D.P. Fagg, D.A. Macedo, Electrochemical assessment of one-step Cu-CGO cermets under hydrogen and biogas fuels, Mater. Lett. 191 (2017) 141–144. https://doi.org/https://doi.org/10.1016/j.matlet.2016.12.087.

[19] M. Sharifi, M. Haghighi, F. Rahmani, S. Karimipour, Syngas production via dry reforming of CH_4 over Co- and Cu-promoted Ni/Al_2O_3-ZrO_2 nanocatalysts synthesized via sequential impregnation and sol-gel methods, J. Nat. Gas Sci. Eng. 21 (2014) 993–1004. https://doi.org/10.1016/j.jngse.2014.10.030.

[20] H. Wu, J.X. Liu, H. Liu, D. He, CO_2 reforming of methane to syngas at high pressure over bi-component Ni-Co catalyst: The anti-carbon deposition and stability of catalyst, Fuel. 235 (2019) 868–877. https://doi.org/10.1016/j.fuel.2018.08.105.

[21] Y. Turap, I. Wang, T. Fu, Y. Wu, Y. Wang, W. Wang, Co–Ni alloy supported on CeO_2 as a bimetallic catalyst for dry reforming of methane, Int. J. Hydrogen Energy. 45 (2020)

6538–6548. https://doi.org/10.1016/j.ijhydene.2019.12.223.

[22] D. San-José-Alonso, J. Juan-Juan, M.J. Illán-Gómez, M.C. Román-Martínez, Ni, Co and bimetallic Ni-Co catalysts for the dry reforming of methane, Appl. Catal. A Gen. 371 (2009) 54–59. https://doi.org/10.1016/j.apcata.2009.09.026.

[23] B.J.M. Sarruf, J.-E. Hong, R. Steinberger-Wilckens, P.E.V. de Miranda, Ceria-Co-Cu-based SOFC anode for direct utilisation of methane or ethanol as fuels, Int. J. Hydrogen Energy. 45 (2020) 5297–5308. https://doi.org/https://doi.org/10.1016/j.ijhydene.2019.04.075.

[24] M. Rezaei, S.M. Alavi, S. Sahebdelfar, Z.F. Yan, Nanocrystalline zirconia as support for nickel catalyst in methane reforming with CO_2, Energy & Fuels. 20 (2006) 923–929. https://doi.org/10.1021/ef050384k.

[25] M.U. Rashid, W.M.A. Wan Daud, H.F. Abbas, Dry reforming of methane: Influence of process parameters - A review, Renew. Sustain. Energy Rev. 45 (2015) 710–744. https://doi.org/10.1016/j.rser.2015.02.026.

[26] B. Cela, D.A. de Macedo, G.L. de Souza, A.E. Martinelli, R.M. do Nascimento, C.A. Paskocimas, NiO–CGO in situ nanocomposite attainment: One step synthesis, J. Power Sources. 196 (2011) 2539–2544. https://doi.org/https://doi.org/10.1016/j.jpowsour.2010.11.026.

[27] A.J.M. Araujo, A.R.O. Sousa, J.P.F. Grilo, L.F.A. Campos, F.J.A. Loureiro, D.P. Fagg, R.P.S. Dutra, D.A. Macedo, Preparation of one-step NiO/Ni-CGO composites using factorial design, Ceram. Int. 42 (2016) 18166–18172. https://doi.org/10.1016/j.ceramint.2016.08.131.

[28] A.J.M. Araújo, J.P.F. Grilo, F.J.A. Loureiro, L.F.A. Campos, C.A. Paskocimas, R.M. Nascimento, D.A. Macedo, Designing experiments for the preparation of Ni-GDC cermets

with controlled porosity as SOFC anode materials: effects on the electrical properties, Ceram. Int. 44 (2018) 23088–23093. https://doi.org/https://doi.org/10.1016/j.ceramint.2018.09.115.

[29] J.B. Usuba, A.J.M. Araújo, E.D. Gonçalves, D.A. Macedo, C. Salvo, M.R. Viswanathan, Flash sintering of one-step synthesized NiO-$Ce_{0.9}Gd_{0.1}O_{1.95}$ (NiO-GDC) composite, Mater. Res. Express. 6 (2019) 125535–125544. https://doi.org/10.1088/2053-1591/ab4f97.

[30] H.C.T. Firmino, A.J.M. Araújo, R.P.S. Dutra, R.M. Nascimento, S. Rajesh, D.A. Macedo, One-step synthesis and microstructure of CuO-SDC composites, Cerâmica. 63 (2017) 52–57. https://doi.org/10.1590/0366-69132017633652088.

[31] J. Estephane, S. Aouad, S. Hany, B. El Khoury, C. Gennequin, H. El Zakhem, J. El Nakat, A. Aboukaïs, E. Abi Aad, CO_2 reforming of methane over Ni-Co/ZSM5 catalysts. Aging and carbon deposition study, Int. J. Hydrogen Energy. 40 (2015) 9201–9208. https://doi.org/10.1016/j.ijhydene.2015.05.147.

[32] H. Eric, M. Timuçin, Equilibrium relations in the system nickel oxide-copper oxide, Metall. Trans. B. 10 (1979) 561–563. https://doi.org/10.1007/BF02662558.

[33] R.J. Moore, J. White, Equilibrium relationships in the systems Li-Co-O and Li-Ni-O, J. Mater. Sci. 9 (1974) 1401–1408. https://doi.org/10.1007/BF00552925.

[34] C.W. Bale, E. Bélisle, P. Chartrand, S.A. Decterov, G. Eriksson, A.E. Gheribi, K. Hack, I.-H. Jung, Y.-B. Kang, J. Melançon, A.D. Pelton, S. Petersen, C. Robelin, J. Sangster, P. Spencer, M.-A. Van Ende, FactSage thermochemical software and databases, 2010–2016, Calphad. 54 (2016) 35–53. https://doi.org/https://doi.org/10.1016/j.calphad.2016.05.002.

[35] G. Bonura, C. Cannilla, F. Frusteri, Ceria-gadolinia supported NiCu catalyst: A suitable system for dry reforming of biogas to feed a solid oxide fuel cell (SOFC), Appl. Catal. B Environ. 121–122 (2012) 135–147. https://doi.org/10.1016/j.apcatb.2012.03.028.

[36] J. Marrero-Jerez, E. Chinarro, B. Moreno, M.T. Colomer, J.R. Jurado, P. Núñez, TPR studies on NiO-CGO composites prepared by combustion synthesis, Ceram. Int. 40 (2014) 3469–3475. https://doi.org/10.1016/j.ceramint.2013.09.083.

[37] J.A. Gómez-Cuaspud, M. Schmal, Effect of metal oxides concentration over supported cordierite monoliths on the partial oxidation of ethanol, Appl. Catal. B Environ. 148–149 (2014) 1–10. https://doi.org/10.1016/j.apcatb.2013.10.036.

[38] X. Wang, W. Wen, J. Mi, X. Li, R. Wang, The ordered mesoporous transition metal oxides for selective catalytic reduction of NO_x at low temperature, Appl. Catal. B Environ. 176–177 (2015) 454–463. https://doi.org/10.1016/j.apcatb.2015.04.038.

[39] J. Marrero-Jerez, A. Murugan, I.S. Metcalfe, P. Núñez, TPR-TPD-TPO studies on CGO/NiO and CGO/CuO ceramics obtained from freeze-dried precursors, Ceram. Int. 40 (2014) 15175–15182. https://doi.org/10.1016/j.ceramint.2014.06.132.

[40] M. Greluk, M. Rotko, S. Turczyniak-Surdacka, Comparison of catalytic performance and coking resistant behaviors of cobalt- and nickel based catalyst with different Co/Ce and Ni/Ce molar ratio under SRE conditions, Appl. Catal. A Gen. 590 (2020) 117334. https://doi.org/https://doi.org/10.1016/j.apcata.2019.117334.

[41] R. Kainuma, M. Ise, C.-C. Jia, H. Ohtani, K. Ishida, Phase equilibria and microstructural control in the Ni-Co-Al system, Intermetallics. 4 (1996) S151–S158. https://doi.org/https://doi.org/10.1016/0966-9795(96)00034-9.

[42] J. Zhang, M.D. Baró, E. Pellicer, J. Sort, Electrodeposition of magnetic, superhydrophobic, non-stick, two-phase Cu–Ni foam films and their enhanced performance for hydrogen evolution reaction in alkaline water media, Nanoscale. 6 (2014) 12490–12499. https://doi.org/10.1039/C4NR03200D.

[43] J.M. Larrain, High temperature thermodynamic properties of copper-nickel alloys, Can.

Metall. Q. 18 (1979) 401–406. https://doi.org/10.1179/cmq.1979.18.4.401.

[44] J. Zhang, H. Wang, A.K. Dalai, Development of stable bimetallic catalysts for carbon dioxide reforming of methane, J. Catal. 249 (2007) 300–310. https://doi.org/10.1016/j.jcat.2007.05.004.

[45] X. Zhang, C. Yang, Y. Zhang, Y. Xu, S. Shang, Y. Yin, Ni-Co catalyst derived from layered double hydroxides for dry reforming of methane, Int. J. Hydrogen Energy. 40 (2015) 16115–16126. https://doi.org/10.1016/j.ijhydene.2015.09.150.

[46] K. Takanabe, K. Nagaoka, K.I. Aika, Improved resistance against coke deposition of titania supported cobalt and nickel bimetallic catalysts for carbon dioxide reforming of methane, Catal. Letters. 102 (2005) 153–157. https://doi.org/10.1007/s10562-005-5848-4.

[47] H. Arbag, S. Yasyerli, N. Yasyerli, G. Dogu, T. Dogu, Enhancement of catalytic performance of Ni based mesoporous alumina by Co incorporation in conversion of biogas to synthesis gas, Appl. Catal. B Environ. 198 (2016) 254–265. https://doi.org/10.1016/j.apcatb.2016.05.064.

[48] S.M. Sidik, S. Triwahyono, A.A. Jalil, Z.A. Majid, N. Salamun, N.B. Talib, T.A.T. Abdullah, CO_2 reforming of CH_4 over Ni-Co/MSN for syngas production: Role of Co as a binder and optimization using RSM, Chem. Eng. J. 295 (2016) 1–10. https://doi.org/10.1016/j.cej.2016.03.041.

[49] O.W. Perez-Lopez, A. Senger, N.R. Marcilio, M.A. Lansarin, Effect of composition and thermal pretreatment on properties of Ni-Mg-Al catalysts for CO_2 reforming of methane, Appl. Catal. A Gen. 303 (2006) 234–244. https://doi.org/10.1016/j.apcata.2006.02.024.